

Hysteresis Compensation in Temperature Response of Fiber Bragg Grating Thermometers Using Dynamic Regression

Zeeshan Ahmed^a

^a*National Institute of Standards and Technology, Physical Measurement Laboratory,
Sensor Science Division, 100 Bureau Drive, Gaithersburg, 20899, MD, USA*

Abstract

In recent years there has been considerable interest in using photonic thermometers such as Fiber Bragg grating (FBG) and silicon ring resonators as an alternative technology to resistance-based legacy thermometers. Although FBG thermometers have been commercially available for decades their metrological performance remains poorly understood, hindered in part by complex behavior at elevated temperatures. In this study we systematically examine the temporal evolution of the temperature response of 14 sensors that were repeatedly cycled between 233 K and 393 K. Data exploration and modelling indicate the need to account for serial-correlation in model selection. Utilizing the coupled-mode theory treatment of FBG to guide feature selection we evaluate various calibration models. Our results indicates that a dynamic regression model can effectively reduce measurement uncertainty due to hysteresis by up to $\approx 70\%$.

Keywords: Photonic thermometry, hysteresis compensation, ARIMA, Couple-mode Theory, Machine Learning, Fiber Bragg gratings

PACS: 0000, 1111

2000 MSC: 0000, 1111

1. Introduction

Temperature measurements encompass almost every aspect of modern life ranging from advanced manufacturing to health screening constituting a multi-billion-dollar enterprise that is expected to continue growing as the

use of temperature sensors proliferate [1] (and refs within). Many thermometry techniques have been developed to meet the varied needs of the user community including resistance-based devices, such as thermistors and platinum resistance thermometers, as well as other sensing modalities including thermocouples, diodes and florescent probes. Standardized manufacturing of metal and semi-conductor based devices ensures an acceptable uncertainty (100 mK to few kelvin) over a given temperature range using nominal coefficients. Tighter uncertainty performance (< 100 mK) requires time consuming calibrations of each individual sensor [2, 3, 4].

The size of the temperature sensor market is a powerful motivator for developing novel technologies targeted towards meeting present and future measurement needs. The existing metrology infrastructure and user expectations of minimum uncertainty metrics along with C-SWaP (cost, size, weight and power) performance requirements represent a formidable barrier to wide-spread adoption of any new temperature measurement technology [5]. As such, any emerging technology is expected to not only provide a novel utility but be backwards compatible with existing infrastructure. Photonic thermometers due to their small size, excellent thermal conductivity and compatibility with telecom infrastructure are expected to meet or exceed user demands[5]. In recent years the photonic thermometry community has largely focused on exploration of novel materials (e.g. silicon[1, 6, 7, 8], silicon nitride[9], diamond, etc[10]), device configurations (Bragg waveguides[11], ring resonators[1, 6], photonic crystal cavities[12] etc) and instrumentation to widen the application window of photonic thermometers beyond metrology labs[6]. Until recently, systematic examination of temperature response of these devices including detailed characterization of measurement uncertainties has been lacking. Several authors have examined the behavior of type-I and type-II fiber Bragg gratings (FBG)¹ sensors at high temperatures and found that the sensors undergo significant hysteresis that is dependent upon both temperature and duration of excursion [13, 14, 15]. These results are broadly in agreement with earlier research on FBG fabrication processes that suggests the fabrication process creates shallow trap states in the bandgap that are "erased" at temperatures higher than 450 K[16, 17, 18, 19]. In ad-

¹grating types refer to photo-sensitivity mechanism used in writing of the grating. Type I rely on UV inscription in photosensitive fibers while Type II gratings are written using localized "damage" caused by two photon absorption

dition, thermally driven ion migration between the fiber core and cladding, glass transition driven stress-strain changes in the fiber, crystallization of α -quartz phase, grating erasure at elevated temperatures and mode mixing are suspected to contribute to measurement uncertainty[17, 18]. At temperatures below 450 K, mechanistic details of thermal hysteresis are unknown[16, 20]. Understanding the mechanism responsible for the hysteresis and quantifying its time-dependent impact on measurement uncertainties are the next steps in the development of FBG thermometers. In this study, we take a physics-informed approach to modeling hysteresis induced changes in the temperature response of FBG sensor. We rely on methods of machine learning and time series forecasting to develop a practical model that can be cost-effectively deployed in industrial setting. We note that elucidation of mechanistic details of hysteresis process i.e. specific changes to the chemical potential or bandgap of the sensor is beyond scope of this study.

2. Experimental

In this study we have utilized commercially available FBG acquired from five different vendors. One set of sensor were coated with a protective layer of polyimide while another set of sensors were coated with an acrylic layer. All other sensors were acquired without the polymeric coating. The fibers were stored in a humidity controlled environment (20% Relative Humidity) prior to use. Each fiber was cleaved such as to leave 2 mm of excess fiber on one side of the sensor, with the other side, 0.5 m long, terminated in a fiber optic coupler. Unless noted otherwise, the sensor was then guided through a T-coupler into a glass tube. The active sensing area of the sensor, at the bottom of the glass tube, was placed inside a through-hole opening (200 μm dia.) of a small copper cylinder. The copper housing provides a strain-free mechanism for anchoring the loose fiber end whilst simultaneously providing a large thermal mass to ensure the the sensor remains in steady equilibrium. The glass tube was then continuously flushed with free-flowing Ar gas to prevent moisture condensation at temperatures below 283 K.

The interrogation system has been described in detail elsewhere[13]. Briefly, the assembled FBG thermometer was placed in a cylindrical Aluminum block (25 mm diameter, 170 mm length). The cylinder has two 150 mm long blind holes (2.5 mm and 6.5 mm diameter) for accommodating a calibrated thermister or platinum resistance thermometer and the assembled FBG sensor, respectively. The calibrated thermometer’s uncertainties over the tempera-

ture range of 233 K to 393 K are below 10 mK. The Aluminum block is placed inside the dry-well calibrator (Fluke 9170) whose temperature is controlled by software written in LabVIEW that cycles the temperature between 233 K to 393 K at preset intervals intervals (typically 5 K). Once the set temperature is achieved, the program allows for an equalisation period (20 mins unless noted otherwise). Following the equalization period the laser (New Focus TLB-6700²) is scanned over a ≤ 2 nm window around the Bragg reflection peak. A small amount of laser power was immediately picked up from the laser output for wavelength monitoring (HighFinesse WS/7) while the rest, after passing through the photonic device via an optical circulator (ThorLabs CIR1550PM-FC), was detected by a large sensing-area power meter (Newport, model 1936-R). Consecutive scans were recorded at each temperature and each sensor was thermally cycled at least three times in each run unless noted otherwise. The recorded data was fitted using a cubic spline to extract peak center, peak height, and peak width as a function of temperature. The assembled dataset contains temperature response of 22 sensors including three quarter-phase gratings and two regenerated-FBG. The r-FBG's response is not included in the analysis presented below. Six other sensors were eliminated from final consideration due to insufficient number of thermal cycles (one or less cycles were successfully collected). Features recorded against temperature include date and time of the measurement, peak center, peak height, full width at half max, area, kurtosis, sensor/grating type, coating, vendor (composite variable standing in for fabrication process variability), time, laser power and experiment type (experiments where number of consecutive scans is 100 or greater are referred to "annealing" as these experiments were designed to detect any slow relaxation process that might be occurring following temperature step). Data exploration was carried out using standard python[21] libraries (pandas[22], seaborn[23], matplotlib[24]) while sklearn sci-kit[25] and statmodels[26] libraries were used for data modeling. A brief discussion of the exploratory data analysis and methodology employed for data modeling is included in the supplemental.

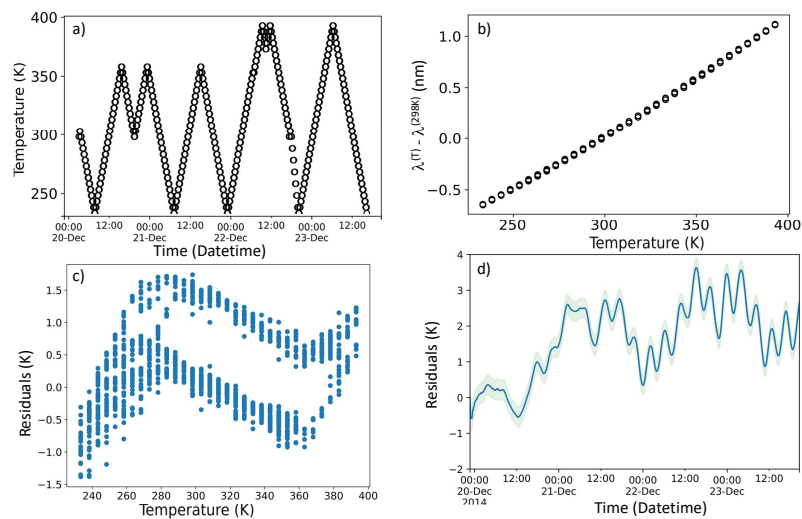


Figure 1: a) Measured temperature cycling profile for sensor S3. b) Measured wavelength detuning vs temperature shows strong quasi-linear dependence that can be modeled as a quadratic function. c) residual of a quadratic fit shows significant departures from normal distribution due to hysteresis. d) time dependence of the residuals from the quadratic fit shown in solid line clearly exhibits a linear increasing trend. The shaded region marks the confidence interval for one-step prediction of AutoRegressive Integrated Moving Average (ARIMA) models trained on the calibration ramp (see discussion for details).

3. Results and Discussion

We explored the complete dataset for possible correlations between temperature and sensor features (see supplemental for details). Exploratory data analysis indicates that besides peak center, which is strongly correlated with temperature, a multitude of features show some degree of correlation with temperature and could be useful in constructing a temperature inference model. Using all of these features together, however would be imprudent. To whittle down the number of candidate features we note that the temperature response of the FBG (and any photonic thermometer in general) relies on the thermo-optic coefficient to transduce temperature changes into the frequency changes[5] (and references within). We therefore, use coupled-model theory treatment of FBG[27, 17, 20] to narrow our feature selection down to only those features that are dependent on the grating refractive index.

The refractive index of the grating can be written as[17]:

$$n = n_{\text{eff}}^o + \Delta n_{\text{eff}}^{\text{mean}} + \Delta n_{\text{eff}}^{\text{mod}} \cos\left(\frac{2\pi z}{\Lambda}\right) \quad (1)$$

where n_{eff}^o is the effective index of the unperturbed fiber, $\Delta n_{\text{eff}}^{\text{mean}}$ and $\Delta n_{\text{eff}}^{\text{mod}}$ are the "DC" (period-average) and "AC" (sinusoidal change over the period) components of the effective index, respectively[17, 27]. The AC component can be evaluated by examining the maximum reflectivity ($\Delta n_{\text{eff}}^{\text{mod}} = \frac{\lambda_B \tanh^{-1}(\sqrt{R_{\text{max}}})}{\pi l}$) or in the case of highly reflective gratings where reflectance does not appear to be a sensitive measure of $\Delta n_{\text{eff}}^{\text{mod}}$, FWHM of the grating spectra can be used. The FWHM of the grating response is known to vary linearly with changes in index modulation. The DC component of the refractive index change of a grating is given by $\Delta n_{\text{eff}}^{\text{mean}} = \frac{\Delta \lambda_B}{2\Lambda}$ and can be measured by tracking the detuning of the grating center wavelength away from the designed wavelength[17, 27, 16].

We therefore restrict ourselves to core group of endogenous variables derived from spectral features- peak center, maximum reflectance, FWHM and kurtosis (stand-in for systematic variations in index along the grating length) to construct potential models. As a baseline model we use simple linear regression between $(\lambda_B - \lambda_B^{(298 \text{ K})})$ and temperature as a quadratic function

²Any mention of commercial products is for informational purposes only; it does not imply recommendation or endorsement by NIST.

(Table 1).³ We designate the first ascending ramp as the calibration run treating it as our training data upon which the regression model is trained. The remaining data is used as "out-of-sample" validation set to not only evaluate how well the trained model generalizes the sensor response but also to characterize and quantify the impact of thermally induced hysteresis. The baseline model indicates an average training error of 513 mK and out-of-sample error of 878 mK. Ten of the 14 sensors examined here show significant thermal hysteresis or ageing effects (training error= 461 mK and out-of-sample error = 1040 mK). In these sensors hysteresis appears to be additive resulting in an offset error that shifts the intercept indicating the overall n_{eff} is increasing as the sensor is exposed to elevated temperature (Fig 1).

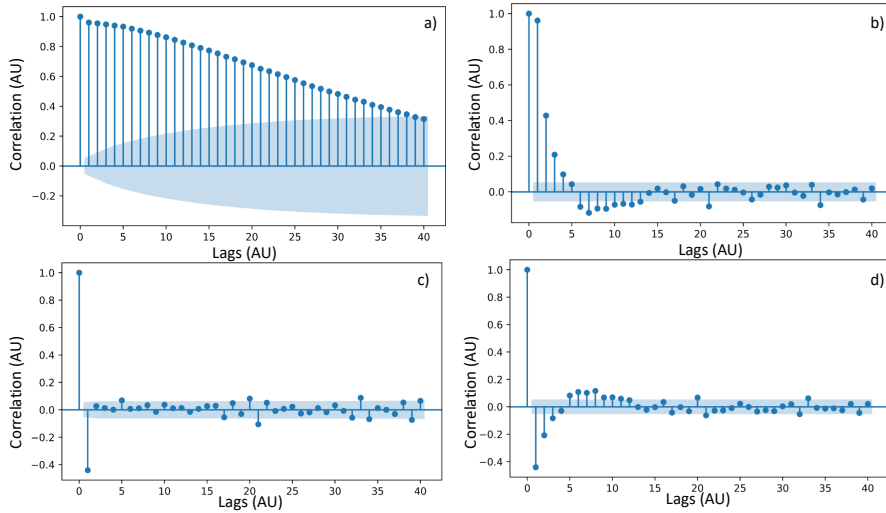


Figure 2: Autocorrelation function (ACF) of S3 sensor's residual is plotted against computed time lags (a) and first-differenced residuals (c) are shown. b and d). Similarly on the right hand panel the partial-autocorrelation function (PACF) plot for S3 sensor's residual (b) and first-differenced residuals (d) are shown. The shaded region marks the uncertainty interval for the auto-correlation coefficients. These plots indicate that hysteresis in S3 can be modeled as (1,1, [1,2,4,5]) process. See supplemental for ACF and PACF plots for every sensor examined in this study.

To improve upon our baseline model's performance we need to account for changes in n_{eff} as the sensor is being thermally cycled. Equation 1 pro-

³We used detuning as the independent parameter since it shows stronger correlation with temperature than peak center. See supplemental for details

vides a framework for breaking down changes in n_{eff} as arising from the AC or DC components of the grating. As noted above the aging effects result in redshift away from the grating wavelength at the start of thermal cycling, behaving as a DC refractive index change process. We model this redshift in baseline grating wavelength by employing a dynamic regression[28] model where the residuals from the training model are used to train a Autoregressive Integrated Moving Average (ARIMA)[28] whose output is added to training /calibration model's output. We examined the auto correlation and partial auto-correlation plots of the residuals to determine a range of (p, d, q) ⁴ parameters for the ARIMA model that are needed to describe the time dependent behavior of the residuals (Fig 2). As shown in Fig 1d the time evolution of residuals is a non-stationary process as indicated by increasing trend. The presence of this trend is also captured by the ACF plot (Fig 2a) which shows positive values for the auto-correlation coefficient that slowly decrease as lags increase. In contrast, the first differenced residual time series' ACF plot is dominated by the first time lag indicating the time series can be transformed into a stationary process by taking the first difference. Furthermore, we note that a lack of significant peaks at longer time lags or multiples of time lags indicates a lack of cyclical behavior in the time evolution of the hysteresis.

The ACF and PACF plots of the difference residuals are used to determine the dominant terms for the autoregressive and moving average terms by selecting the highest time time lags correlation coefficients significantly larger than the calculated uncertainty. These parameters were then further optimized by maximizing the log-likelihood of the fit. Overall our exploration of parameter space indicates that simple ARIMA models containing a linear trend ($d = 1$) and short term moving average ($q < 10$) and autoregressive term ($p < 2$) is sufficient to capture long term changes in the residual across all sensors. That is, the long-term drift in FBG can be described as consisting of three components: a slow linear drift, a short-term memory (< 300 s) and a white noise component. Caution should be exercised when using the order of ARIMA terms to draw insights into physical processes responsible for the observed hysteresis. Given that changes in Bragg wavelength are due to changes in the n_{eff} , we interpret the linear trend as indicating the n_{eff}

⁴ p, d, q refer to the order of autoregressive, integrative and moving average processes. Hence a (1,1,1) process would be described as being autoregressive in the first order with a simple linear trend and a moving average of one. The first order difference i.e. linear trend correction is necessary to make the time series stationary

of the sensor shows a slow, linear increase as thermal cycles progress. The origin(s) of the short-term memory effect is difficult to assign. It is likely that this term is capturing short term process such as modal noise due to thermal or strain relaxation in the fiber or short-term correlation in the temperature control loop of the bath.

As shown in Table 1 the mean uncertainty for one-step prediction is only 265 mK while uncertainty when using dynamic prediction⁵ over the out-of-sample set is 623 mK which is 69% and 41% lower than the baseline model, respectively. We note that while the model performs well over the short-term (one-step forecast), uncertainty in the forecast grows with the horizon. As such these models are most appropriate over finite horizons. For metrology problems requiring infinite horizons, state-space models or long-short term memory (LSTM) models[29] that incorporate device physics, chemistry and thermal history may be more appropriate.

We evaluated the possibility that hysteresis maybe accounted by changes in the AC component i.e. the observed hysteresis may derive in part from the grating contrast erasure. As noted above, changes in the AC component of index proportionally impact the amplitude and width of the resonance spectra. In order to incorporate the AC index change into our model, we therefore incorporate additional features (time normalized amplitude, fractional FWHM and kurtosis)⁶ into a multivariate regression model employing L2 regularization ($\alpha = 0.000001$), multi-layer preceptrons (MLP) with one or two hidden layers employing sigmodial activation ([100x1] or [5x1],[3x1] , respectively) and a hidden-state-like model where amplitude, fractional width and kurtosis are transformed and regressed to predict peak center detuning, $(\lambda_B - \lambda_B^{(298K)})$, which in turn is added as a feature along with measured peak center detuning to a multivariate regression model. As shown in Table 2 the resulting models fail to improve upon the baseline model, generally performing worse. Failure of these models to accurately compensate for hysteresis suggests that while spectral features other than the peak center show temporal changes, these changes are neither linearly correlated with temperature nor the observed peak center. Hysteresis in FBG can be adequately modeled

⁵see supplemental for discussion of differences between one-step vs dynamic prediction

⁶kurtosis is a stand-in variable for non-uniform changes in AC index along the fiber axis i.e. it reports on the dephasing of the grating index contrast. time-normalized amplitude and fractional width are used in place of amplitude and FWHM, respectively, because they show stronger correlations with peak center.

as a DC-only process.

Table 1: Results of Dynamic Regression Model for Hysteresis Compensation

Sensor	Hysteric	Training error	Out of sample error	One step error	Dynamic pred. error	Uncorrected error over dynamic range
S1	Yes	0.1369	2.106	0.32	0.79	1.9
S2	Yes	0.352	1.553	0.09	0.78	1.45
S3	Yes	0.4683	1.06	0.15	0.42	0.69
S4	Yes	0.774	0.88	0.34	0.48	0.81
S5	Yes	0.4576	0.761	0.17	0.42	0.598
S6	Yes	0.2485	0.749	0.25	0.6	0.67
S7	Yes	0.5381	0.808	0.34	0.55	2.35
S8	Yes	0.8184	1.269	0.63	1.05	1.08
S9	Yes	0.4565	0.81	0.15	0.73	0.54
S10	Yes	0.3622	0.4	0.21	0.41	0.41
S11	No	0.7529	0.6985	0.29	0.47	0.73
S12	No	0.5255	0.5745	0.16	0.6	0.66
S13 ^a	No	0.445	0.447	0.29	0.48	0.45
S13 ^b	No	0.424	0.431	0.28	0.57	0.43
S14	No	0.9336	0.6275	0.25	0.85	0.83
Mean ^c		0.461	1.04	0.265	0.623	1.05
Mean ^d		0.513	0.878	0.261	0.613	0.9

^a input power less than 10 microwatt

^b input power 2.5 mW

^c mean of hysteretic sensors only

^d mean of all sensors

Table 2: Modeling Hysteresis using an Expanded set of Spectral Features as Inputs to the Calibration Model

Model	Training Error (K)	Out of Sample Error (K)
Baseline ^a	0.513	0.878
Hidden-state-like ^b	0.627	6.66
Lasso ^c	1.13	6.31
MLP ^d	10.42	22.98
MLP ^e	7.88	21.14

^a peak center detuning is the only input

^b fractional width, kurtosis and amplitude are used to predict wavelength detuning. this prediction is used as an input to a regression model along with measured wavelength detuning to infer temperature

^c input features include wavelength detuning, kurtosis, fractional width and area, alpha = 0.000001;

^d hidden layers [5*3], alpha = 0.0001

^e hidden layer [100], alpha = 0.0001

4. Summary

Long term hysteresis or ageing effects in photonic thermometers [13, 14, 15, 12] represent a significant measurement science challenge to the adoption of photonic thermometry in-lieu of resistance thermometers. In this study we demonstrate that guided by device physics we can deploy proven statistical techniques to model the ageing effects and successfully reduce the measurement uncertainty by up to 70%. Our work here serves as a motivation to develop first principles based thermo-optic coefficient models that can be co-deployed with ARIMA models in Kalman filter like predictor-corrector algorithms to reduce measurement uncertainty and gain mechanistic understanding of processes driving long and short term drift in sensor characteristics.

5. Acknowledgments

Author thanks Dan Samarov, Gilad Kusne, Tobias Herman and Tyrus Berry for helpful discussion. This work was funded by NIST-on-a-chip (NOAC) initiative.

6. Disclosures

The author declares no conflicts of interest.

References

- [1] H. Xu, M. Hafezi, J. Fan, J. M. Taylor, G. F. Strouse, Z. Ahmed, Ultra-sensitive chip-based photonic temperature sensor using ring resonator structures, *Opt. Express* 22 (3) (2014) 3098–3104. doi:10.1364/OE.22.003098.
URL <http://opg.optica.org/oe/abstract.cfm?URI=oe-22-3-3098>
- [2] H. Preston-Thomas, The international temperature scale of 1990 (its-90), *Metrologia* 27 (1) (1990) 3–10.
- [3] Consultative Committee for Thermometry under the auspices of the International Committee for Weights and Measures, *mise en pratique for the definition of the kelvin in the SI*, <https://www.bipm.org/en/publications/mises-en-pratique> (2019).

- [4] B. W. Mangum, G. F. Strouse, W. F. Guthrie, R. Pello, M. Stock, E. Renaot, Y. Hermier, G. Bonnier, P. Marcarino, K. S. Gam, K. H. Kang, Y.-G. Kim, J. V. Nicholas, D. R. White, T. D. Dransfield, Y. Duan, Y. Qu, J. Connolly, R. L. Rusby, J. Gray, G. J. Sutton, D. I. Head, K. D. Hill, A. Steele, K. Nara, E. Tegeler, U. Noatsch, D. Heyer, B. Fellmuth, B. Thiele-Krivoj, S. Duris, A. I. Pokhodun, N. P. Moiseeva, A. G. Ivanova, M. J. de Groot, J. F. Dubbeldam, Summary of comparison of realizations of the ITS-90 over the range 83.8058 k to 933.473 k: CCT key comparison CCT-k3, *Metrologia* 39 (2) (2002) 179–205. doi:10.1088/0026-1394/39/2/7.
URL <https://doi.org/10.1088/0026-1394/39/2/7>
- [5] Z. Ahmed, Role of quantum technologies in reshaping the future of temperature metrology, *Measurement: Sensors* 18 (2021) 100308. doi:<https://doi.org/10.1016/j.measen.2021.100308>.
URL <https://www.sciencedirect.com/science/article/pii/S2665917421002713>
- [6] R. Eisermann, S. Krenek, G. Winzer, S. Rudtsch, Photonic contact thermometry using silicon ring resonators and tuneable laser-based spectroscopy, *tm - Technisches Messen* 88 (10) (2021) 640–654. doi:doi:10.1515/teme-2021-0054.
URL <https://doi.org/10.1515/teme-2021-0054>
- [7] S. Janz, R. Cheriton, D.-X. Xu, A. Densmore, S. Dedyulin, A. Todd, J. H. Schmid, P. Cheben, M. Vachon, M. K. Dezfouli, D. Melati, Photonic temperature and wavelength metrology by spectral pattern recognition, *Opt. Express* 28 (12) (2020) 17409–17423. doi:10.1364/OE.394642.
URL <http://opg.optica.org/oe/abstract.cfm?URI=oe-28-12-17409>
- [8] C. Zhang, G. Kang, Y. Xiong, T. Xu, L. Gu, X. Gan, Y. Pan, J. Qu, Photonic thermometer with a sub-millikelvin resolution and broad temperature range by waveguide-microring fano resonance, *Opt. Express* 28 (9) (2020) 12599–12608. doi:10.1364/OE.390966.
URL <http://opg.optica.org/oe/abstract.cfm?URI=oe-28-9-12599>

- [9] C. Zhang, G.-G. Kang, J. Wang, S. Wan, C.-H. Dong, Y.-J. Pan, J.-F. Qu, Photonic thermometer by silicon nitride microring resonator with milli-kelvin self-heating effect, *Measurement* 188 (2022) 110494. doi:<https://doi.org/10.1016/j.measurement.2021.110494>. URL <https://www.sciencedirect.com/science/article/pii/S0263224121013774>
- [10] J. A. Smith, P. Hill, C. Klitis, M. Sorel, P. A. Postigo, L. Weituschat, M. D. Dawson, M. J. Strain, High precision diamond-on-gan photonic thermometry enabled by transfer printing integration, in: *OSA Advanced Photonics Congress 2021*, Optica Publishing Group, 2021, p. IM1A.4. doi:[10.1364/IPRSN.2021.IM1A.4](https://doi.org/10.1364/IPRSN.2021.IM1A.4). URL <http://opg.optica.org/abstract.cfm?URI=IPRSN-2021-IM1A.4>
- [11] N. N. Klimov, S. Mittal, M. Berger, Z. Ahmed, On-chip silicon waveguide bragg grating photonic temperature sensor, *Opt. Lett.* 40 (17) (2015) 3934–3936. doi:[10.1364/OL.40.003934](https://doi.org/10.1364/OL.40.003934). URL <http://opg.optica.org/ol/abstract.cfm?URI=ol-40-17-3934>
- [12] N. Klimov, T. Purdy, Z. Ahmed, Towards replacing resistance thermometry with photonic thermometry, *Sensors and Actuators A: Physical* 269 (2018) 308–312. doi:<https://doi.org/10.1016/j.sna.2017.11.055>. URL <https://www.sciencedirect.com/science/article/pii/S0924424717318940>
- [13] Z. Ahmed, J. Filla, W. Guthrie, J. Quintavalle, Fiber bragg grating based thermometry, *NCSLI Measure* 10 (4) (2015) 28–31. doi:[10.1080/19315775.2015.11721744](https://doi.org/10.1080/19315775.2015.11721744).
- [14] D. Grobncic, C. Hnatovsky, S. Dedyulin, R. B. Walker, H. Ding, S. J. Mihailov, Fiber bragg grating wavelength drift in long-term high temperature annealing, *Sensors* 21 (4) (2021). doi:[10.3390/s21041454](https://doi.org/10.3390/s21041454). URL <https://www.mdpi.com/1424-8220/21/4/1454>
- [15] R. Eisermann, S. Krenek, T. Habisreuther, P. Ederer, S. Simonsen, H. Mathisen, T. Elsmann, F. Edler, D. Schmid, A. Lorenz, A. A. F. Olsen, Metrological characterization of a high-temperature hybrid sensor using thermal radiation and calibrated sapphire fiber bragg grating

- for process monitoring in harsh environments, *Sensors* 22 (3) (2022).
doi:10.3390/s22031034.
URL <https://www.mdpi.com/1424-8220/22/3/1034>
- [16] T. Erdogan, V. Mizrahi, P. J. Lemaire, D. Monroe, Decay of ultraviolet-induced fiber bragg gratings, *Journal of Applied Physics* 76 (1) (1994) 73–80. arXiv:<https://doi.org/10.1063/1.357062>, doi:10.1063/1.357062.
URL <https://doi.org/10.1063/1.357062>
- [17] H. Patrick, S. L. Gilbert, A. Lidgard, M. D. Gallagher, Annealing of bragg gratings in hydrogen-loaded optical fiber, *Journal of Applied Physics* 78 (5) (1995) 2940–2945. arXiv:<https://doi.org/10.1063/1.360753>, doi:10.1063/1.360753.
URL <https://doi.org/10.1063/1.360753>
- [18] D. P. Hawn, The effects of high temperature and nuclear radiation on the optical transmission of silica optical fibers, Ph.D. thesis, The Ohio State University (2012).
- [19] A. Munko, S. Varzhel', S. Arkhipov, A. Gribaev, K. Konnov, M. Belikin, The study of the thermal annealing of the bragg gratings induced in the hydrogenated birefringent optical fiber with an elliptical stress cladding, *Journal of Physics: Conference Series* 735 (2016) 012015. doi:10.1088/1742-6596/735/1/012015.
URL <https://doi.org/10.1088/1742-6596/735/1/012015>
- [20] S. Pal, J. Mandal, T. Sun, K. T. V. Grattan, Analysis of thermal decay and prediction of operational lifetime for a type i boron-germanium codoped fiber bragg grating, *Appl. Opt.* 42 (12) (2003) 2188–2197. doi:10.1364/AO.42.002188.
URL <http://opg.optica.org/ao/abstract.cfm?URI=ao-42-12-2188>
- [21] G. Van Rossum, F. L. Drake, *Python 3 Reference Manual*, CreateSpace, Scotts Valley, CA, 2009.
- [22] Wes McKinney, *Data Structures for Statistical Computing in Python*, in: Stéfan van der Walt, Jarrod Millman (Eds.), *Proceedings of the*

- 9th Python in Science Conference, 2010, pp. 56 – 61. doi:10.25080/Majora-92bf1922-00a.
- [23] M. L. Waskom, seaborn: statistical data visualization, *Journal of Open Source Software* 6 (60) (2021) 3021. doi:10.21105/joss.03021.
URL <https://doi.org/10.21105/joss.03021>
- [24] J. D. Hunter, Matplotlib: A 2d graphics environment, *Computing in Science & Engineering* 9 (3) (2007) 90–95. doi:10.1109/MCSE.2007.55.
- [25] F. Pedregosa, G. Varoquaux, A. Gramfort, V. Michel, B. Thirion, O. Grisel, M. Blondel, P. Prettenhofer, R. Weiss, V. Dubourg, J. Vanderplas, A. Passos, D. Cournapeau, M. Brucher, M. Perrot, E. Duchesnay, Scikit-learn: Machine learning in Python, *Journal of Machine Learning Research* 12 (2011) 2825–2830.
- [26] S. Seabold, J. Perktold, statsmodels: Econometric and statistical modeling with python, in: 9th Python in Science Conference, 2010, pp. 92–96.
- [27] T. Erdogan, Fiber grating spectra, *Journal of Lightwave Technology* 15 (8) (1997) 1277–1294. doi:10.1109/50.618322.
- [28] R. J. Hyndman, G. Athanasopoulos, *Forecasting: Principles and Practice*, 2nd edition, OTexts, Melbourne, Australia, 2018.
- [29] S. Hochreiter, J. Schmidhuber, Long Short-Term Memory, *Neural Computation* 9 (8) (1997) 1735–1780. arXiv:<https://direct.mit.edu/neco/article-pdf/9/8/1735/813796/neco.1997.9.8.1735.pdf>, doi:10.1162/neco.1997.9.8.1735.
URL <https://doi.org/10.1162/neco.1997.9.8.1735>

1. Methodology

1.1. Data Exploration

The data exploration process began with examination of Pearson coefficient heatmaps (Fig SP1) and pairplots (Fig SP 2) of all continuous variables over the entire dataset and then parsed over each of the non-categorical variable. Furthermore, each feature's temperature and time dependence was examined separately to ascertain their behavior over time and temperature history. Data exploration indicates that against temperature the following feature show positive correlations: peak center, kurtosis, (fractional) peak width and grating type. No significant correlations were observed between temperature and the following features: time, amplitude, laser power and fringe visibility. Furthermore, we observe peak detuning (a feature created by subtracting the value of peak center value at 293.15 K at the start of measurements from all subsequent measurements) shows stronger correlation with temperature (0.91) as compared to peak center (0.77).

The temporal evolution of each feature during thermal cycling was examined for each sensor. Thermal time history and attendant changes in peak center and fractional peak width for sensors S6 and S7 are shown in Fig SP 3 and SP 4, respectively. We note that the time histories of the two exemplar sensors show significant differences in the magnitude of changes, suggesting the hysteresis evolution is sensitive to the sensor's history which may include manufacturing conditions, thermal annealing and other variables. Furthermore, as shown in Fig SP 3 and SP 4, changes in spectra-derived features are slow and cumulative, rising above the prevailing measurement noise only over long time periods. As shown in Fig SP 5, the Allen deviation (ADEV) plots for sensor S5 and S7 show that the measurement uncertainty at any given temperature is dominated by $1/f$ noise as evidenced by a linear decrease in variance with integration time. Based on these results we conclude that peak center drift due to hysteresis either occurs outside the observation times used in this study¹ or that the impact of these changes on measurement variance is smaller than the impact of other processes over the observation times used for each temperature measurement. Based on these results and

¹note that we allow an equilibration time of upto 20 mins once the temperature bath reaches the set temperature to eliminate any thermal gradients in the sensor. Hysteretic changes maybe be occurring during this deadtime or over time scales much longer than the mintues to hours long observation times used here

33 previous literature[1, 2] we conclude that the process responsible for hystere-
34 sis is likely similar to slow random diffusion of a polymer on a rough energy
35 landscape marred by shallow traps. During thermal annealing the grating
36 appears to be dephasing- as suggested by changes in peak center and width-
37 which suggests that during annealing some of the shallow traps are wiped out
38 and their population transferred to deeper traps. As the effective bandgap
39 of the material redshifts, the refractive index of the optical fiber increases
40 resulting in an offset error of the temperature calibration. In our subsequent
41 analysis we therefore treat the impact of hysteresis as being a cumulative
42 effect of the temperature ramp.

43 *1.2. Modelling Methodology*

44 The serial correlations or memory effects introduced by hysteresis (see
45 discussion above), pose significant challenges to model evaluation. In any
46 model training endeavor where the goal is to develop a deployable, generalized
47 model, it is important to appropriately balance the bias-variance tradeoff[3].
48 In sensor literature often the focus is on the training error e.g. the mean
49 square error of fitting a function to the entire dataset is reported. Only
50 optimizing the training error runs the risk of over-fitting the data creating
51 a model that reduces residuals when fitted to the data it was trained on
52 but fails poorly when new data is introduced. To balance the tendency of
53 models to over-learn, the data is divided between a training and validation
54 set (sometimes alternatively referred to as testing set). The model is initially
55 trained on the training set and subsequently evaluated on the validation set.
56 The goal is to choose a model that minimizes both the training and validation
57 scores i.e. a generalizable model that accounts for significant trends in the
58 data without learning the noise.

59 The presence of serial correlations in the data however make simple train-
60 test split strategy- e.g. randomly selecting and setting aside 30% of the data
61 points for testing set- inappropriate. As shown in table 1, for 9 out of 14
62 sensors a train-test split results in out-of-sample errors (validation error) that
63 are either similar or smaller than the training errors suggesting the noise is
64 not appropriately balanced between the two datasets. Similar results are
65 seen for k-fold cross validation (CV) where the data set is randomly broken
66 into k sets. The k-fold CV approach has the benefit of minimizing the impact
67 of outliers on the fit[3]. A common solution to the serial correlation problem
68 is to implement time-series cross validation (TSCV)[4, 3]. Such an approach,
69 however, makes it difficult to interperate the model in terms that are common

70 in metrology e.g. hysteresis. We, therefore, implement a version of TSCV by
71 dividing the data between the first up ramp (training set) and subsequent
72 data (testing set). This ramp-by-ramp division of the data is appropriate
73 because as shown above the effects of changes driving hysteresis are only
74 significant over long time periods. Our approach divides the dataset in two
75 long time periods, allowing us to isolate the uncertainty introduced by long
76 term drift. The model evaluation on the training set is carried out using k-fold
77 cross validation (k=5)[3]. Consistent with previous literature[5] we find that
78 a quadratic function vastly outperforms a first order model, reducing MSE
79 by $\approx 75\%$. We note that cubic functions show a slight improvement (13%)
80 over quadratic function. For the purposes of this study, however, we have
81 chosen the simpler quadratic function to model the temperature-wavelength
82 (peak center) relationship staying consistent with previous literature[6, 5].
83 A detailed evaluation of different models where model complexity (number
84 of free parameters) is weighed against its validation error is the subject of a
85 forthcoming manuscript.

Table 1: Training and out-of-sample (validation) error in train-test split evaluation of a first order regression model

Sensor	Training Error (K)	Out of Sample Error (K)
S1	2.107	1.984
S2	1.78	1.67
S3	1.930	1.851
S4	2.314	2.291
S5	0.357	0.341
S6	0.994	1.023
S7	2.116	2.099
S8	2.196	2.057
S9	2.301	2.275
S10	2.418	2.472
S11	2.330	2.344
S12	1.947	1.937
S13 ^a	2.138	2.161
S13 ^b	2.322	2.571
S14	2.228	2.279

^a $1\mu W$ input power

^b $2.5mW$ input power

87 *1.2.1. Dynamic Regression*

88 As discussed in the manuscript we employed ARIMA models in a dy-
89 namic regression scheme to compensate for the long-term drift in the sensor
90 refractive index due to hysteresis. As noted in the manuscript, the (p, d, q)
91 terms for each sensor is determined by examining the ACF and PCF plots of
92 the residuals and first-difference residuals [4]. The time dependent temper-
93 ature changes, residuals and ACF and PCF plots for each sensor are shown
94 below. We note that the ARIMA models are evaluated by computing their
95 performance for one-step and dynamic prediction. The one-step prediction
96 refers to outputs of the dynamic regression model where the validation set is
97 introduced one-sequential time step at a time and prediction generated using
98 the last time step i.e. predictions are restricted to short time-horizons. In
99 the case of dynamic prediction, the entire validation set is evaluated at once
100 i.e. the input to ARIMA model (residuals) are restricted to only the calibra-
101 tion/testing set. The results of one-step prediction represents the best-case
102 performance that can be expected from these models. The dynamic predic-
103 tion results, on the other hand, provides a measure of long-term (few weeks)
104 performance of these models.

105 **References**

- 106 [1] T. Erdogan, V. Mizrahi, P. J. Lemaire, D. Monroe, Decay of ultraviolet-
107 induced fiber bragg gratings, *Journal of Applied Physics* 76 (1) (1994)
108 73–80. arXiv:<https://doi.org/10.1063/1.357062>, doi:10.1063/1.
109 357062.
110 URL <https://doi.org/10.1063/1.357062>
- 111 [2] H. Patrick, S. L. Gilbert, A. Lidgard, M. D. Gallagher, Annealing of bragg
112 gratings in hydrogen-loaded optical fiber, *Journal of Applied Physics*
113 78 (5) (1995) 2940–2945. arXiv:<https://doi.org/10.1063/1.360753>,
114 doi:10.1063/1.360753.
115 URL <https://doi.org/10.1063/1.360753>
- 116 [3] G. James, D. Witten, T. Hastie, R. Tibshirani, *An Introduction to Statis-*
117 *tistical Learning: with Applications in R.*, Springer, New York, USA, 2013.
118 doi:10.1007/978-1-4614-7138-7.
- 119 [4] R. J. Hyndman, G. Athanasopoulos, *Forecasting:Principles and Practice*,
120 2nd edition, OTexts, Melbourne, Australia, 2018.

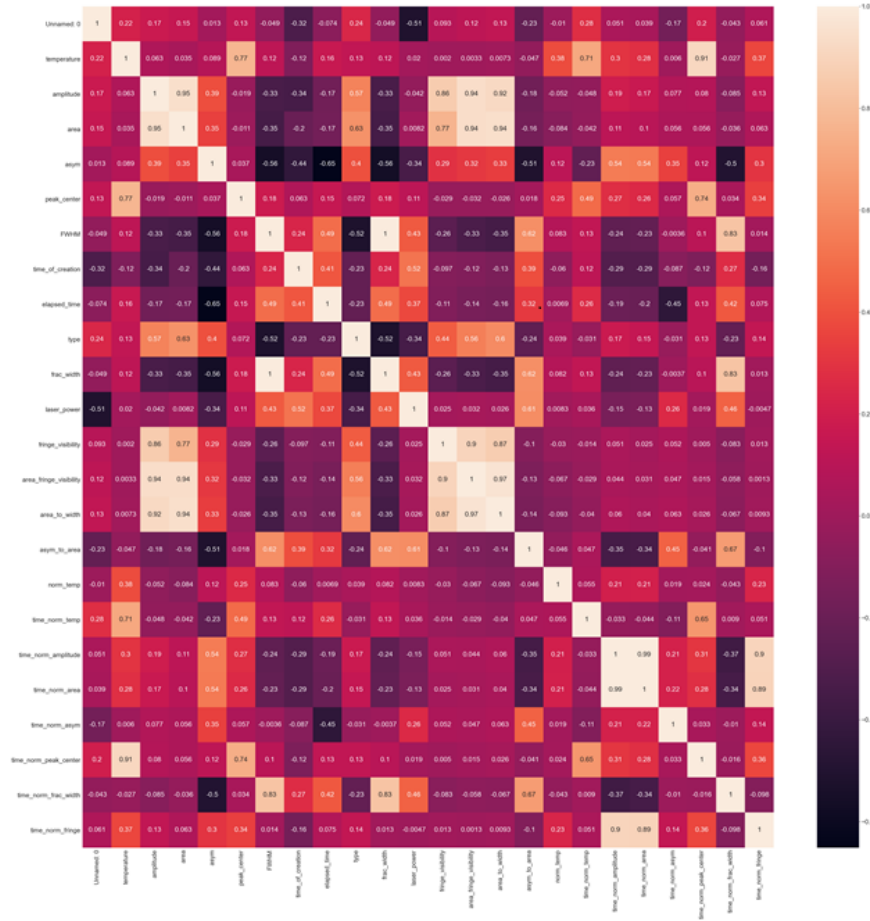


Figure 1: Heatmap of Pearson correlation coefficient for non-categorical variables for the entire data of FBG temperature response

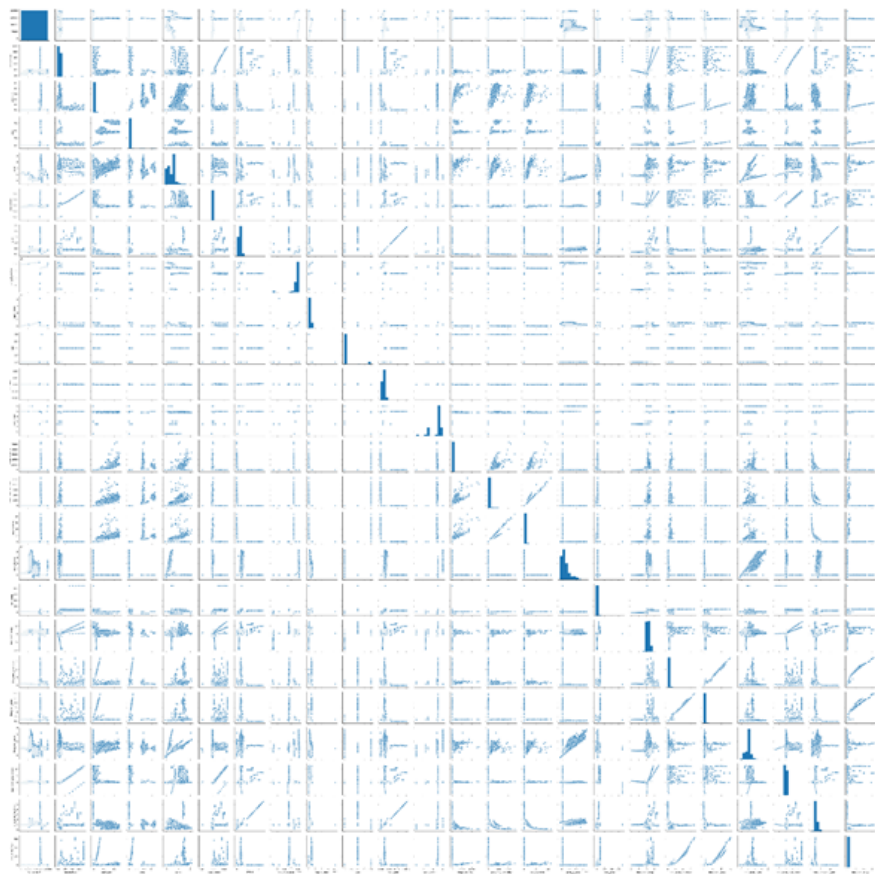


Figure 2: Pairplots of all non-categorical variables over the entire data set

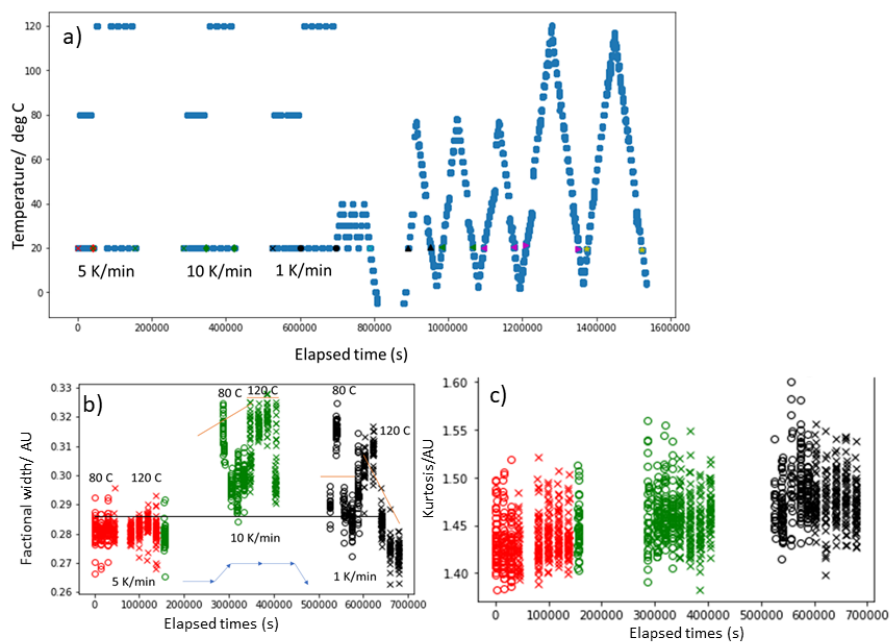


Figure 3: a) Thermal cycling history of sensor S6 includes different heating rates and temperature excursions. At 293 K, time and temperature dependent evolution of fractional width b) and Kurtosis c) in sensor S6 shows significant memory effects

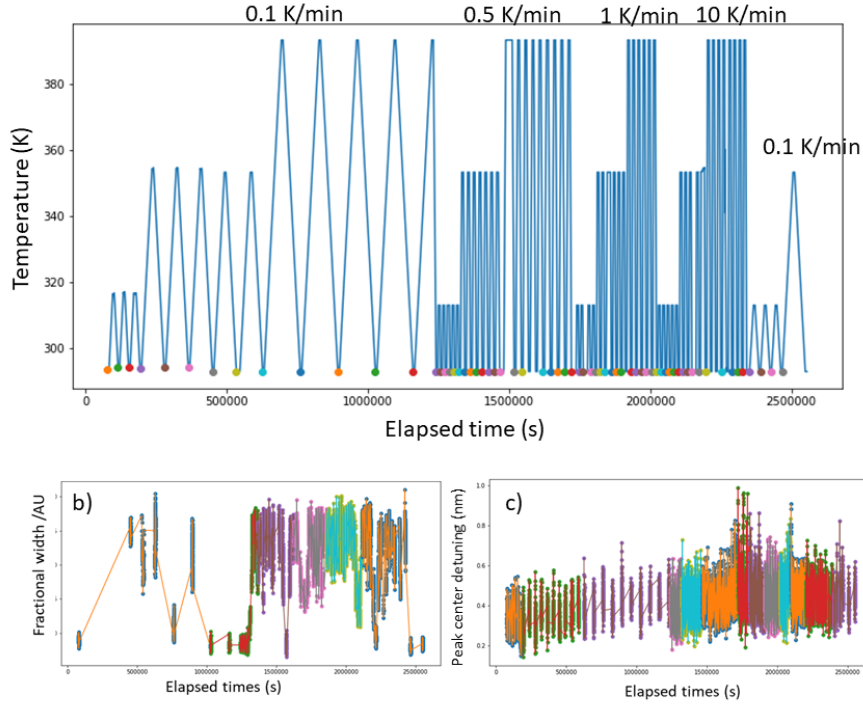


Figure 4: a) Thermal cycling history of sensor S7 includes different heating rates and temperature excursions. At 293 K, the cumulative effective of thermal treatment's effect on the fractional width (a) and peak center detuning (b) can be seen.

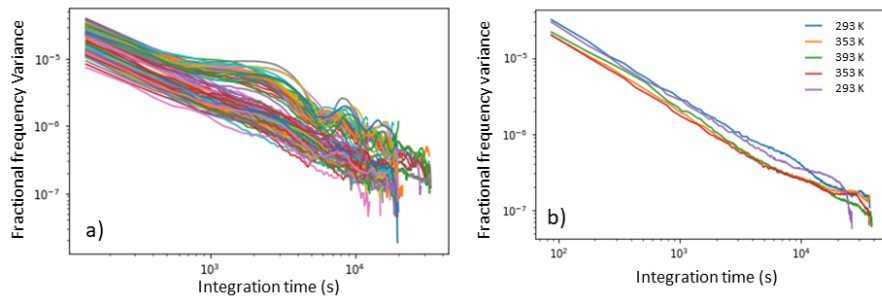


Figure 5: a) Allen deviation plots for sensor S7 at every temperature between 283 K and 393 K recorded over three thermal cycles. Temperature was incremented in 5 K steps b) Allen deviation plots for sensor S5 at 293 K (start), 353 K , 393 K from the ramp-up and 293 K (ramp-down) are shown. For both sensors, regardless of temperature, we observe a dominant linear trend indicating the measurement noise is dominated by 1/f noise process

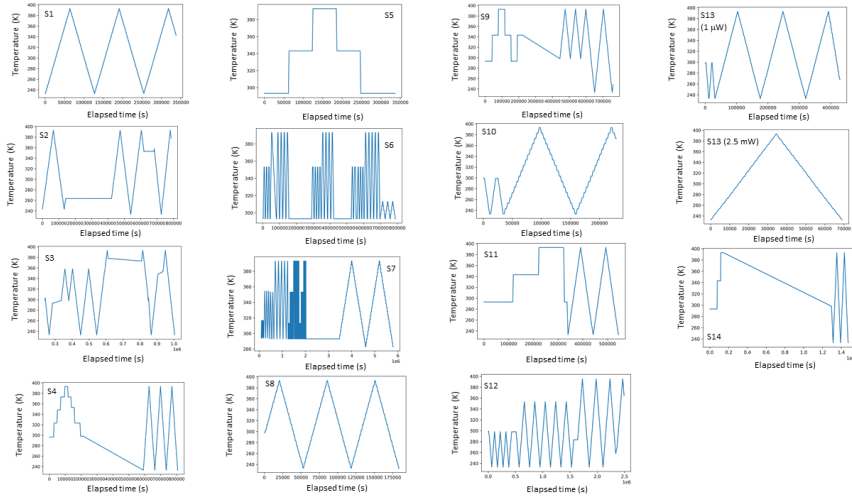


Figure 6: Time history of temperature changes for each sensor is shown

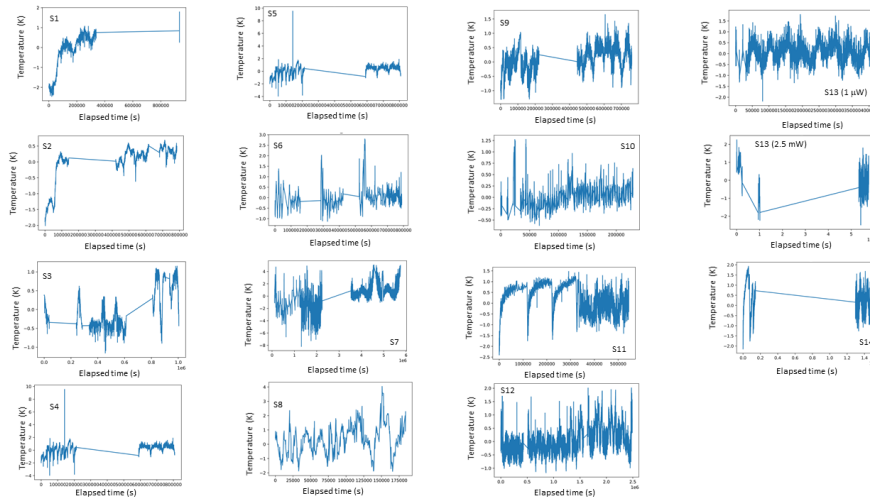


Figure 7: Temporal evolution of residuals calculated from regression model for each sensor are shown

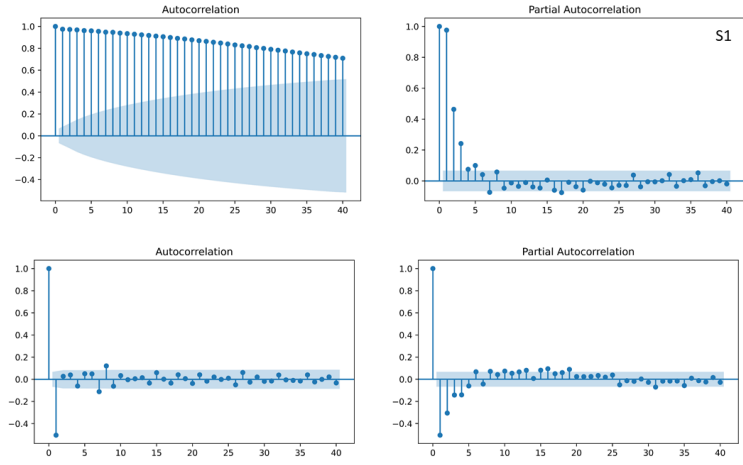


Figure 8: ACF and PCF plots calculated from the residuals (top) and first-difference residuals plot (bottom) for S1 are shown.

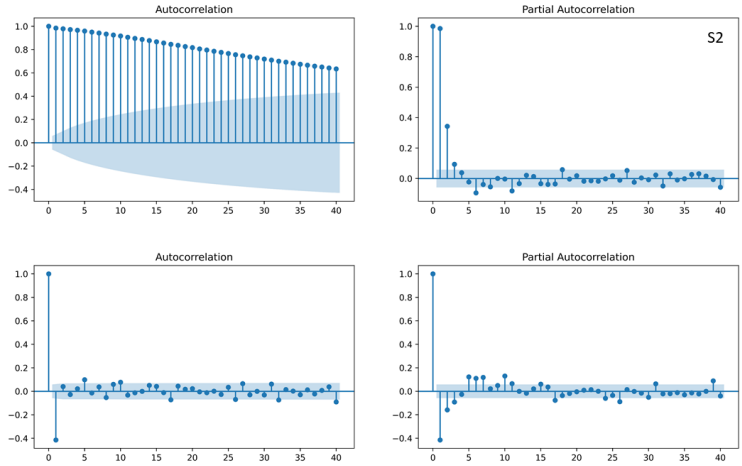


Figure 9: ACF and PCF plots calculated from the residuals (top) and first-difference residuals plot (bottom) for S2 are shown.

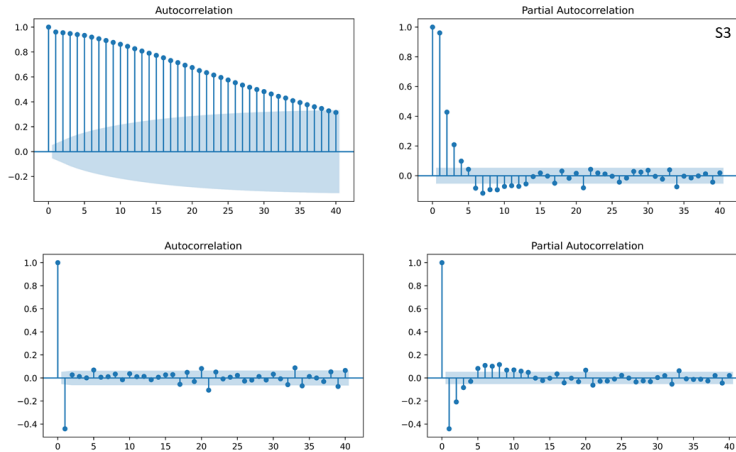


Figure 10: ACF and PCF plots calculated from the residuals (top) and first-difference residuals plot (bottom) for S3 are shown.

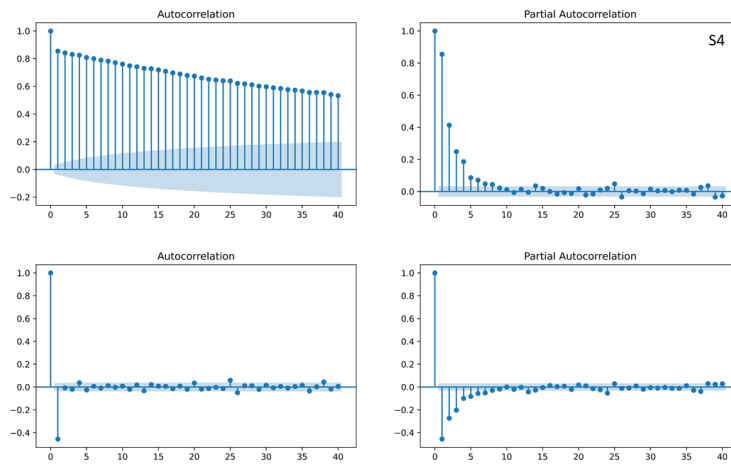


Figure 11: ACF and PCF plots calculated from the residuals (top) and first-difference residuals plot (bottom) for S4 are shown.

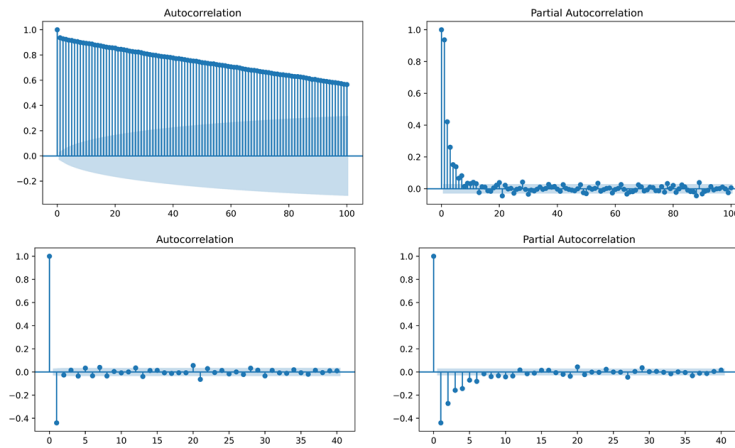


Figure 12: ACF and PCF plots calculated from the residuals (top) and first-difference residuals plot (bottom) for S5 are shown.

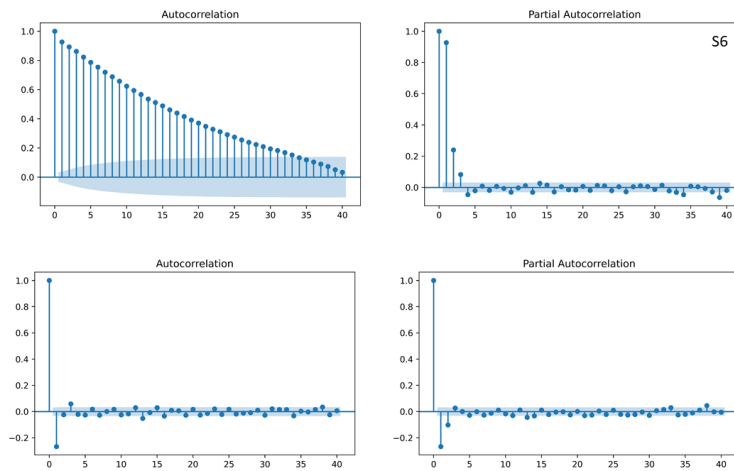


Figure 13: ACF and PCF plots calculated from the residuals (top) and first-difference residuals plot (bottom) for S6 are shown.

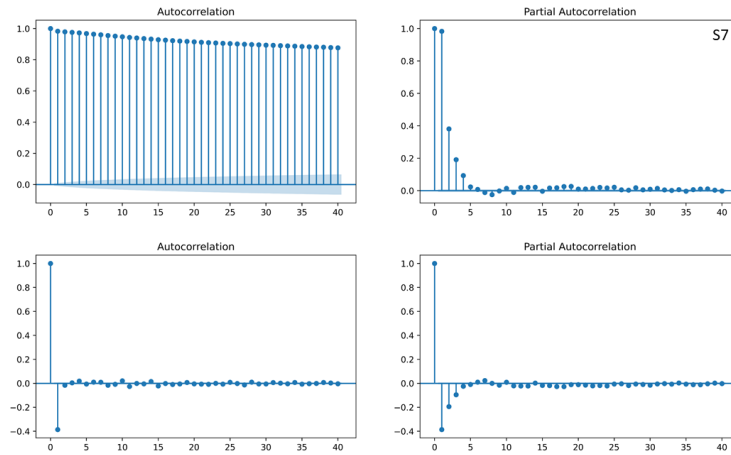


Figure 14: ACF and PCF plots calculated from the residuals (top) and first-difference residuals plot (bottom) for S7 are shown.

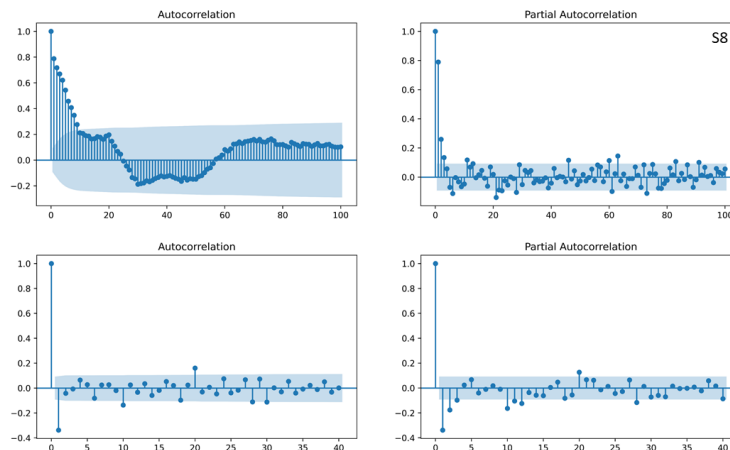


Figure 15: ACF and PCF plots calculated from the residuals (top) and first-difference residuals plot (bottom) for S8 are shown.

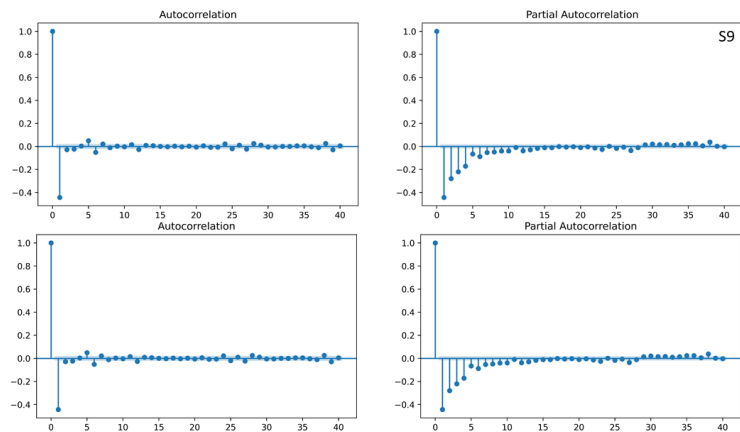


Figure 16: ACF and PCF plots calculated from the residuals (top) and first-difference residuals plot (bottom) for S9 are shown.

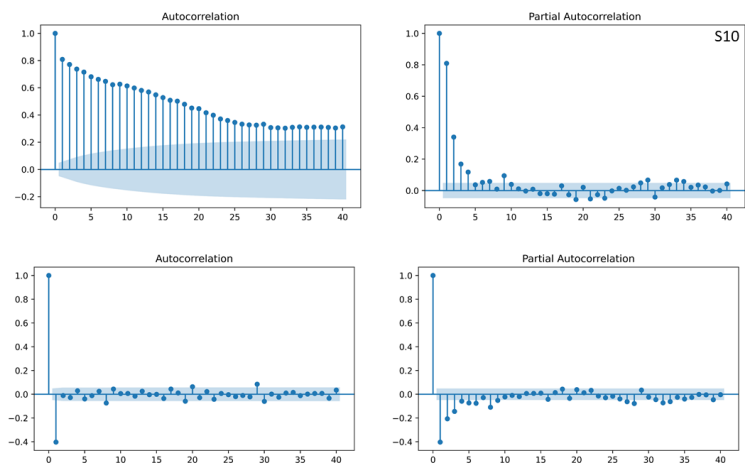


Figure 17: ACF and PCF plots calculated from the residuals (top) and first-difference residuals plot (bottom) for S10 are shown.

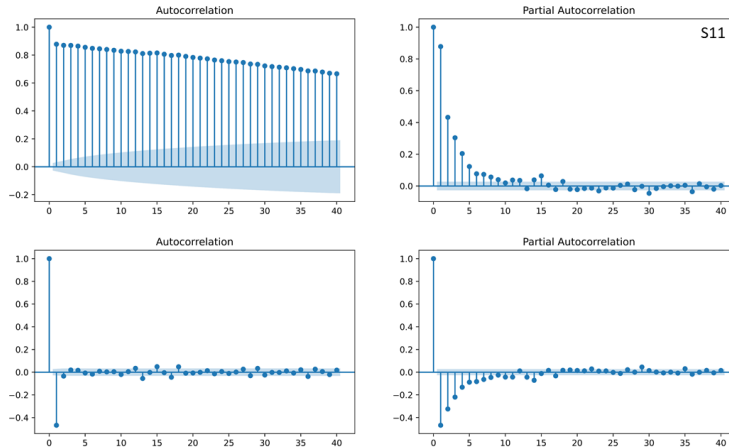


Figure 18: ACF and PCF plots calculated from the residuals (top) and first-difference residuals plot (bottom) for S11 are shown.

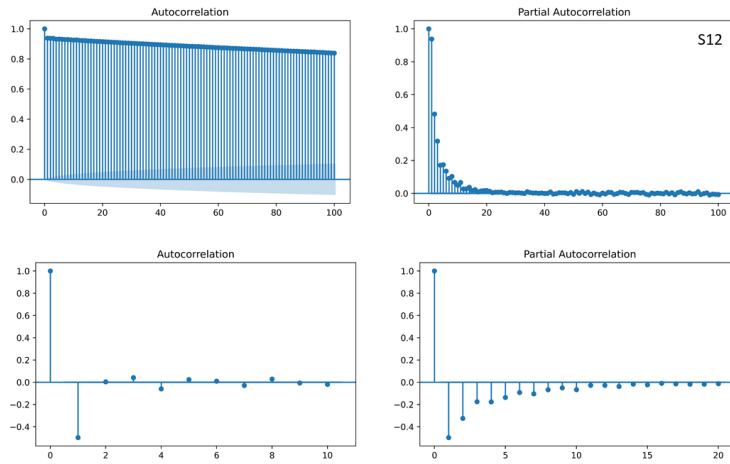


Figure 19: ACF and PCF plots calculated from the residuals (top) and first-difference residuals plot (bottom) for S12 are shown.

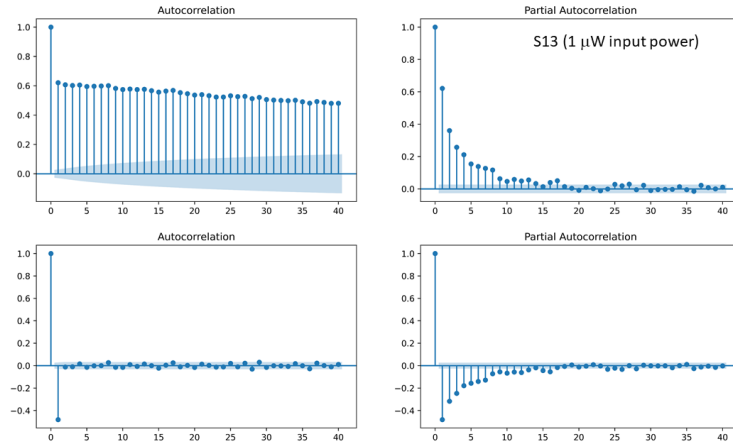


Figure 20: ACF and PCF plots calculated from the residuals (top) and first-difference residuals plot (bottom) for S13 at $1\mu W$ of input power are shown.

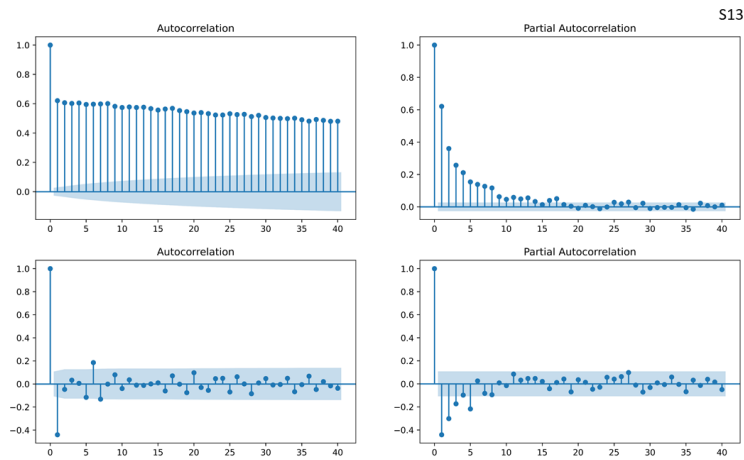


Figure 21: ACF and PCF plots calculated from the residuals (top) and first-difference residuals plot (bottom) for S13 at 2.5 mW of input power are shown.

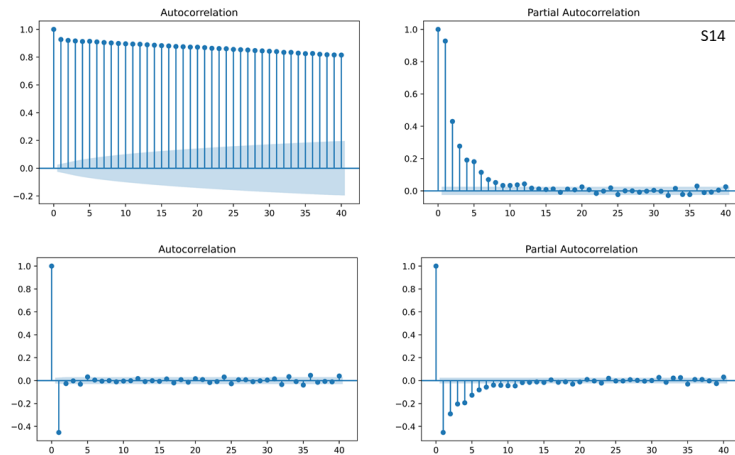


Figure 22: ACF and PCF plots calculated from the residuals (top) and first-difference residuals plot (bottom) for S14 are shown.

- 121 [5] G. M. Flockhart, R. R. Maier, J. S. Barton, W. N. MacPherson, J. D.
 122 Jones, K. E. Chisholm, L. Zhang, I. Bennion, I. Read, P. D. Foote,
 123 Quadratic behavior of fiber bragg grating temperature coefficients, *Ap-
 124 plied optics* 43 (13) (2004) 2744–2751.
- 125 [6] Z. Ahmed, J. Filla, W. Guthrie, J. Quintavalle, Fiber bragg grat-
 126 ing based thermometry, *NCSLI Measure* 10 (4) (2015) 28–31. doi:
 127 10.1080/19315775.2015.11721744.

128

129

130

Supplemental: Hysteresis Compensation in
Temperature Response of Fiber Bragg Grating
Thermometers Using Dynamic Regression

131

Zeeshan Ahmed^a

*^aNational Institute of Standards and Technology, Physical Measurement Laboratory,
Sensor Science Division, 100 Bureau Drive, Gaithersburg, 20899, MD, USA*
